

Identification of infrasonic and seismic components of tremors in single-station records: application to the 2013 and 2018 events at Ioto Island, Japan

Aika K Kurokawa (✉ kurokawa@bosai.go.jp)

National Research Institute for Earth Science and Disaster Prevention <https://orcid.org/0000-0002-3113-4752>

Mie Ichihara

Earthquake Research Institute, University of Tokyo

Full paper

Keywords: Volcanic tremor, Infrasound, Vertical ground motion, Spectral ratio, Ioto

Posted Date: September 4th, 2020

DOI: <https://doi.org/10.21203/rs.3.rs-34753/v2>

License:  This work is licensed under a Creative Commons Attribution 4.0 International License.

[Read Full License](#)

Version of Record: A version of this preprint was published on November 9th, 2020. See the published version at <https://doi.org/10.1186/s40623-020-01302-2>.

1 **Identification of infrasonic and seismic components of tremors in**
2 **single-station records: application to the 2013 and 2018 events**
3 **at Ioto Island, Japan**

4 Aika K. Kurokawa, National Research Institute for Earth Science and Disaster Resilience,
Tennodai 3-1, Tsukuba, Ibaraki 305-0006, Japan, kurokawa@bosai.go.jp
Mie Ichihara, Earthquake Research Institute, University of Tokyo, ichihara@eri.u-tokyo.ac.jp

6 **Abstract**

7 Infrasonic stations are sparse at many volcanoes, especially those on remote islands and those with less
8 frequent eruptions. When only a single infrasound station is available, the seismic-infrasonic
9 cross-correlation method has been used to extract infrasound from wind noise. However, it does not
10 work with intense seismicity and sometimes mistakes ground-to-atmosphere signals as infrasound. This
11 paper proposes a complementary method to identify the seismic component and the infrasonic
12 component using a single microphone and a seismometer. We applied the method to estimate the
13 surface activity on Ioto Island. We focused on volcanic tremors during the phreatic eruption on April 11,
14 2013, and during an unconfirmed event on September 12, 2018. We used the spectral amplitude ratios
15 of the vertical ground motion to the pressure oscillation and compared those for the tremors with those
16 for known signals generated by volcano-tectonic earthquakes and airplanes flying over the station. We
17 were able to identify the infrasound component in the part of the seismic tremor with the 2013 eruption.
18 On the other hand, the tremor with the unconfirmed 2018 event was accompanied by no apparent
19 infrasound. We interpreted the results that the infrasound with the 2013 event was excited by the vent
20 opening or the ejection of ballistic rocks, and the 2018 event was not an explosive eruption either on the
21 ground or in the shallow water. If there was any gas (and ash) emission, it might have occurred gently
22 undersea. As the method uses the relative values of on-site records instead of the absolute values, it is
23 available even if the instrument sensitivity and the station site effects are poorly calibrated.

24 **Keywords**

25 Volcanic tremor, Infrasound, Vertical ground motion, Spectral ratio, Ioto Island

26 **Introduction**

27 Eruption in isolated volcanic islands are becoming the focus of attention for their significant growth, as
28 in the case of Nishinoshima (Maeno et al. 2016; Kaneko et. al 2019), and for the hazardous nature, as
29 in Anak Krakatau (Williams et al. 2019; Perttu et al. 2020) and White Island more recently (Dempsey
30 et al. 2020). The existence of abundant water tends to cause hazardous eruptions like phreatomagmatic
31 and phreatic explosions (Mastin and Witter 2000; Stix and Moor 2018). It is often the case in isolated

32 islands, the occurrences, the times, and the sequences of eruptions are not identified due to the lack of
33 observations. The detection is particularly hard for small but frequent eruptions because signals are not
34 strong enough to reach the global monitoring network.

35 Infrasound is generated by activity such as opening vent and emission of volcanic gas and rocks so
36 that it is useful to distinguish the volcano's surface activity from underground processes (e.g. Ripepe et
37 al. 2018). When infrasound data during an eruption is available only from a single station, it is difficult
38 to distinguish the eruption signals from wind noise. To detect infrasound signals, Ichihara et al. (2012)
39 proposed a cross-correlation analysis between the pressure oscillation and ground motion signals, which
40 has been applied successfully with some improvements (e.g. Cannata et al. 2013; Matoza and Fee 2014;
41 Nishida and Ichihara 2015; Ichihara 2016; Yukutake et al. 2018). McKee et al. (2018) extended the
42 method by incorporating the phase shift and the seismic particle motion to estimate the infrasound back
43 azimuth. However, the method is not applicable when the volcano is seismically very active, and the
44 seismic signal dominates infrasound signal in the seismometer record. Moreover, if the ground velocity
45 associated with the seismic wave is significantly large, it generates pressure perturbation that is noticeable
46 in the infrasound data (Kim et al. 2004; Watada et al. 2006). Such a ground-to-atmosphere signal can
47 be mistaken as an infrasound signal when only a single infrasound station exists.

48 Ioto Island is an isolated volcanic island of which seismicity is regularly intense (Ueda et al. 2018).
49 At Ioto Island, phreatic eruptions frequently occur due to the high geothermal activity (Notsu et al.
50 2005), and the volcanic activity is pronounced not only on the ground but also undersea detected by
51 remote hydrophones (Matsumoto et al. 2019). In this situation where the volcanic activity is very high
52 throughout the island, there is a need to monitor eruptions and its temporal changes.

53 This study aims to identify volcanic infrasound using a single pair of seismometer and microphone
54 at Ioto Island. By comparing the data of the tremors associated with the 2013 eruption and the
55 unconfirmed 2018 event with those of volcano-tectonic earthquakes and human-made infrasound, we
56 distinguish tremors including infrasound and purely seismic tremors.

57 **Volcanic Activities at Ioto Island in 2013 and 2018**

58 Ioto Island (Iwo-jima) is one of the most active isolated volcanic islands in Japan, located approximately
59 1200 km south of Tokyo and belongs to the Izu-Bonin-Mariana island arc. The island, about 8 km \times 4 km
60 in size with the highest elevation of 170 m, is just the summit part of a stratovolcano rising about 2000

61 m from the sea floor. Eruptions sometimes occur under the sea and are detected by remote hydrophones
62 (Matsumoto et al. 2019). The seismic activity is intense and a large-scale uplift has continued for centuries
63 (Kaizuka et al. 1985; Ueda et al. 2018). Although minor phreatic explosions seem to occur frequently at
64 various points in the island (Corwin and Foster 1959; Notsu et al. 2005; Ueda et al. 2018), most of them
65 have not been confirmed in terms of their occurrences, times, and source vents.

66 An eruption occurred at about 16:00 JST (all times hereafter are in JST, which is UTC+0900)
67 on April 11, 2013, has been observed from the ground and the sky and recorded by time-identified
68 photographs (Japan Meteorological Agency 2013). It occurred at Million dollar hole (Fig. 1) with dark
69 smoke of 400 m height and large ballistic rocks while the seismic activity and crustal movement were less
70 intensive. It accompanied a volcanic tremor lasting about 9 min from 15:59 on April 11.

71 Another activity seems to have occurred in shallow water near the Okinahama coast (Fig. 1) on
72 September 12, 2018, though the only evidence is water spouts with heights of 5-10 m observed at around
73 11:00 on the day (Japan Meteorological Agency 2018). It was preceded by predominant uplift and high-
74 frequency seismicity for a few weeks. Data from local seismometers and remote hydrophones during the
75 period indicates that frequent undersea eruptions associated with volcano-tectonic earthquakes occurred
76 (Matsumoto et al. 2019). From September 12 to 13, the number of long-period events and volcanic
77 tremors increased while that of volcano-tectonic earthquakes decreased (Japan Meteorological Agency
78 2018). Then, the volcanic activity gradually declined. We investigate the 2018 activity in comparison
79 with the confirmed case of the 2013 eruption.

80 **Data and Methods**

81 **Data**

82 We used the records at the three seismic stations in Ioto Island (Fig. 1). IOCD station of the Japan
83 Meteorological Agency (JMA) is equipped with a velocity seismometer (L-4C, 1 Hz, Sercel Inc.) and an
84 infrasonic microphone (TYPE7144, > 0.1 Hz, Aco Co., Ltd.) having a horizontal separation of 7.6 m
85 and a vertical difference of 1.5 m. IJSV and IJTV stations operated by the National Research Institute
86 for Earth Science and Disaster Resilience (NIED) have velocity seismometers (J21-3D, 1 Hz, Mitsutoyo
87 Corporation). The sampling frequency of all the instruments is 100 Hz. Note that the IOCD is the
88 only infrasonic station in Ioto Island and the nearest seismic station to the vent of 2013 eruption and
89 the location where the water spouts were observed in the 2018 activity. The distances of IOCD to these

90 possible sources are 1.03 and 0.94 km, respectively.

91 This study focuses on two tremor events (Fig. 2); TR1 on April 11, 2013, and TR2 on September 12,
92 2018 (TR2 included the three sequences). TR1 coincided with the 2013 eruption (Japan Meteorological
93 Agency 2013). On the other hand, the volcanic activity associated with TR2 is unknown, though it is
94 the most prominent tremors during the 2018 activity (Japan Meteorological Agency 2018). We expect to
95 determine whether TR2 accompanied infrasound or not by the combined analyses of the data from the
96 seismometer and the microphone at IOCD.

97 Figure 2 shows the wave traces and the spectrograms of the whole analyzed periods for TR1 and
98 TR2. In both TR1 and TR2, the seismic velocity amplitude is the largest at IOCD and the smallest at
99 IJTV. The relation is consistent with the relative distances between the stations and the active areas as in
100 Fig. 1. Although the seismic site-effects should be considered, strictly speaking, it implies the amplitude
101 attenuation with distance from the source. The spectrograms indicate that the dominant frequencies of
102 TR1 and TR2 range in 1-10 and 1-5 Hz, respectively. TR1 is overlapped by an airplane noise, which has
103 a harmonic feature with dominant frequencies about 18 and 36 Hz (Fig. 2c).

104 **Cross-correlation Analysis**

105 We performed a cross-correlation analysis between the vertical ground velocity and the microphone data
106 at IOCD. The method distinguishes infrasonic signals from wind noise, and helps detect eruption events
107 in the situation where only one microphone is available (Ichihara et al. 2012). With the distance between
108 the seismometer and the microphone, d , of 7.7 m, the range of frequency, f , should satisfy the relation:
109 $v/3 < f \cdot d \leq \alpha$ (v is the wind velocity, and α is the sound velocity), which guarantees that d is smaller
110 than the infrasound wave lengths and larger than correlation lengths of wind noise (Shields 2005). We
111 assumed that α is 340 m/s. We also considered that v is smaller than the maximum wind speed of 11.8
112 m/s observed at Chichijima island about 280 km to the north of Ioto Island in April 2013 and September
113 2018. Then, the relation is rewritten as $0.5 < f \leq 44.2$ Hz. Therefore, we used the frequency band of
114 1-10 Hz. The cross-correlation coefficient (CC) was calculated for the delay time of the vertical ground
115 velocity to the microphone data from -0.5 to 0.5 s by use of a 5-s time window sliding every 1 s.

116 **Seismic- and Infrasonic- Spectral Ratio**

117 Seismic waves propagating in the ground and infrasound waves propagating in the atmosphere individually
118 generate both of ground motion and pressure oscillation. Therefore, it is not apparent whether an
119 oscillation recorded by a single sensor (either a seismometer or a microphone) is a seismic- or infrasonic-

120 wave. The basic theory for the acoustic coupling between the ground and the atmosphere is described in
 121 Appendixes A and B. We here only present the essential point.

122 When infrasound propagates along the ground surface, the vertical ground velocity, $w_p(f)$, induced
 123 by the infrasonic pressure wave, $p_{in}(f)$, is given in the frequency domain by

$$w_p(f) = \frac{\alpha}{2(\lambda + \mu)} \frac{\lambda + 2\mu}{\mu} p_{in}(f) e^{-i\pi/2}, \quad (1)$$

124 where (λ, μ) are Lamé's constants for the ground (Ben-Menahem and Singh 1981). The effective values
 125 of Lamé's constants vary with stations and depend on frequency because they are influenced by the
 126 shallow structure of the ground and topography (Langston 2004; Nishida and Ichihara 2015). Empirically,
 127 $|w_p(f)/p_{in}(f)|$ ranges 0.1-10 $\mu\text{m}\cdot\text{s}^{-1}/\text{Pa}$ (e.g. Langston 2004; Matoza and Fee 2014; Nishida and Ichihara
 128 2015; Ichihara 2016).

129 On the other hand, when the vertical ground velocity due to the propagating seismic wave, $w_{in}(f)$,
 130 induces local air pressure perturbations, $p_w(f)$, in a homogeneous fluid medium assuming that the time
 131 scale of the vertical motion is short compared with the acoustic cut-off period in the atmosphere, the
 132 relation is formulated as

$$p_w(f) = \rho\alpha w_{in}(f), \quad (2)$$

133 where ρ is the density of air (Cook 1971; Donn and Posmentier 1964; Kim et al. 2004). There exist
 134 records of ground-to-atmosphere signals excited by large earthquakes, which have a good agreement with
 135 the theory (Kim et al. 2004; Watada et al. 2006). In these cases, $|w_{in}(f)/p_w(f)|$ is as large as 3000
 136 $\mu\text{m}\cdot\text{s}^{-1}/\text{Pa}$. Because the spectral amplitude ratio of seismometer data to microphone data is significantly
 137 different depending on whether the wave is seismic or infrasonic, we use it to distinguish the waves. For
 138 convenience, the observed spectral amplitude ratio will be referred to as $(w/p)_{obs}$.

139 We calculated $(w/p)_{obs}$ for each of TR1 and TR2 in the following steps. ① Power spectral densities
 140 (PSDs) of the seismic data (the vertical component) and infrasonic record were individually calculated
 141 in a 10-s window sliding with 5-s overlapping for the periods shown in Fig. 2. ② The wind is the most
 142 critical noise in the infrasound record, which has significant power in low frequencies below 1 Hz (Fee and
 143 Garces 2007). Therefore, we focused on the frequency range above 1 Hz in searching for volcanic signals.
 144 For each time window, we calculated the powers of the infrasound data in high- and low- frequency

145 bands, $E_h = \int_1^{10} \text{PSD}(f)df$ and $E_l = \int_{0.5}^1 \text{PSD}(f)df$, respectively. If $\sqrt{E_h} > 3\sqrt{E_l}$, we employed the time
146 window. ③ For each of TR1 and TR2, we averaged the PSDs over the time windows selected in ② to
147 obtain the mean PSDs, $P_W(f)$ and $P_P(f)$, for the seismic and infrasonic data, respectively. Then, we
148 obtained the spectral amplitude ratio, $(w/p)_{obs} = \sqrt{P_W(f)/P_P(f)}$. ④ We also evaluated mean PSDs
149 for the background noise spectra, $P_W^b(f)$ and $P_P^b(f)$, for seismic- and infrasonic-data, respectively. We
150 searched the background time windows from 14:00-17:00 of April 11, 2013, for TR1 and from 0:00-24:00 of
151 September 8, 2018, for TR2. It would be better to use time windows as close as possible to the occurrence
152 time of the target signal to obtain a reliable background level. However, because of the intense volcanic
153 seismicity during the 2018 activity, it was hard to extract adequate background data near the signal.
154 Therefore we used the time windows before the days of the intense activity. When the infrasonic PSDs
155 above 1 Hz are smaller than $10^{-3} \text{ Pa}^2/\text{Hz}$ and the seismic PSDs are below $5 (\mu\text{m}\cdot\text{s}^{-1})^2/\text{Hz}$ in a time
156 window, we regarded it as a background noise window. We took 100 time windows for each of TR1 and
157 TR2, and averaged the PSDs to obtain $P_W^b(f)$ and $P_P^b(f)$. ⑤ The mean PSDs for the signals ($P_W(f)$
158 and $P_P(f)$ obtained in ③) and those for background ($P_W^b(f)$ and $P_P^b(f)$ evaluated in ④) were compared.
159 The meaningful frequency bands were defined by the following condition:

$$\frac{P_W(f) - a_w P_W^b(f)}{a_w P_W^b(f)} > 10, \quad \frac{P_P(f) - a_p P_P^b(f)}{a_p P_P^b(f)} > 10. \quad (3)$$

160 The background noise levels were adjusted by a_w and a_p so that the mean PSDs for the signal and the
161 noise were equal at 0.5 Hz. Wind noise power generally increases in the lower frequency. The frequency
162 of 0.5 Hz is below the signal's dominant frequency range and above the sensor's low-frequency limit.
163 Namely, $a_w = P_W(0.5)/P_W^b(0.5)$, and $a_p = P_P(0.5)/P_P^b(0.5)$. The shifting was applied to remove the
164 effect of temporal change in wind noise. The spectral characteristics of the tremors and the background
165 noises obtained by the method are compared in Fig. 3.

166 For reference, we evaluated $(w/p)_{obs}$ for known infrasonic- and seismic-signals, which are airplane
167 sound propagating in the atmosphere (PN) and seismic waves generated by tectonic earthquakes (EQ).
168 The method was similar to the above. For PN, we analyzed the data from 16:00-17:00 of April 11, 2013
169 and from 10:00-11:00 of September 12, 2018, in which we found clear airplane signals in the spectrograms.
170 As PN signals had powers in high frequency, we changed the frequency range in step ① to 10-40 Hz,
171 and the threshold of Eq. (3) to 30 in step ⑤. In step ②, 6 and 54 time windows met the requirement

172 in 2013 and 2018 data, respectively. As regards EQ, we used 51 and 118 tectonic earthquakes that
 173 occurred in Ioto Island in March-April 2013 and September 2018, respectively. The timetables are shown
 174 in Supplementary materials referring to the NIED catalog. Because many earthquakes occurred in Ioto
 175 Island, signals that had good cross-correlation between the seismometer and the microphone (the CC
 176 larger than 0.6) and peak seismic amplitudes larger than $50 \mu\text{m/s}$ at IOCD were selected. Twenty-second
 177 records from 10 s before the peaks were used for calculating $P_W(f)$ and $P_P(f)$. Then, we performed step
 178 ⑤ to select the meaningful frequency band.

179 Results

180 The seismic- and infrasonic- records and the seismic-to-infrasonic CCs in the analyzed periods for TR1
 181 and TR2 are shown in Fig. 4. Figure 5 shows results of the same analysis for the reference signals (PN
 182 and EQ). If both of the seismometer and the microphone record infrasound propagating along the ground
 183 surface, the CC would have a positive peak near $\tau = 1/(4f_0)$, a negative peak near $\tau = -1/(4f_0)$, and a
 184 node at $\tau = 0$ (Ichihara et al. 2012; Yukutake et al. 2018). We observe some change in the pattern for
 185 a few minutes from 16:00 in TR1 (Fig. 4c). However, its maximum CC value is not so high as that for
 186 PN (e.g. from 10:15 to 10:17 in Fig. 5c), which is close to 1. The low CC value of TR1 suggests that the
 187 major contribution to the signal recorded by the seismometer is not infrasonic origin but seismic waves.
 188 Nevertheless, the subtle pattern change may be due to the coexistence of infrasound with the seismic
 189 tremor of TR1. On the other hand, CCs of TR2 and EQ share a feature with a positive peak around $\tau =$
 190 0 and a negative peak in $\tau > 0$ as shown in Figs. 4d and 5d. It suggests a seismic origin for TR2 signal
 191 in both seismic- and infrasonic- data.

192 Figure 6 compares the mean power spectra and $(w/p)_{obs}$ of TR1 and TR2 against PN and EQ. Figure
 193 6c shows that $(w/p)_{obs}$ of TR1 is closer to that of PN than EQ. The infrasonic amplitude is too large
 194 to be generated by the observed ground velocity. On the other hand, both powers of the seismic and
 195 infrasonic data during TR2 are comparable to the ground-to-atmosphere signal of EQ (Figs. 4b, 5b, and
 196 6b). These results support the inference from CC that a pressure wave accompanied TR1 but not TR2.
 197 Although the existence of infrasound for TR2 cannot be completely ruled out, it would have been so weak
 198 to be obscured by the observed noise in the infrasound data ($< 0.1 \text{ Pa}$), if it happened.

199 Discussion

200 The values of $(w/p)_{obs}$

201 The spectral ratios of seismic data to infrasonic data, $(w/p)_{obs}$, were calculated to discuss the volcanic
202 activities with TR1 and TR2, as presented in Fig. 6c and 6d. Here, we consider if the values of $(w/p)_{obs}$
203 are reasonable, focusing on the reference signals of EQ and PN. EQ that is seismic wave has $(w/p)_{obs}$ in
204 agreement with the theoretical value of ground-to-atmosphere signals (Kim 2004; Watada et al., 2006),
205 which is given in Eq. (2) and indicated as the dotted line in the figures. PN is acoustic wave and has
206 $(w/p)_{obs}$ ranging 1-10 $\mu\text{m}\cdot\text{s}^{-1}/\text{Pa}$. The range is included in the observed values for atmosphere-to-ground
207 signals, 0.1-10 $\mu\text{m}\cdot\text{s}^{-1}/\text{Pa}$, from various sources like volcanoes (Nishida and Ichihara 2015; Ichihara 2016;
208 Matoza and Fee 2014) and thunder (Lin and Langston 2007, 2009a).

209 We have presented Eq. (1) as the theoretical amplitude ratio for atmosphere-to-ground signals. It
210 assumes that the atmospheric wave is propagating along the ground surface at speed much lower than
211 the seismic waves, and the ground and the atmosphere are homogeneous half-spaces (Ben-Menahem and
212 Singh 1981). Equation (1) with $(w/p)_{obs} \sim 10 \mu\text{m}\cdot\text{s}^{-1}/\text{Pa}$ yields the shear modulus of ~ 26 MPa using
213 $\lambda = \mu$. The shear modulus is equivalent to that of loose-packing sand or clay (Lo Presti et al. 1997),
214 and Chidorigahara area in Ioto Island, including IOCD station, is composed almost entirely of poorly-
215 consolidated volcanic sands and gravels (Corwin and Foster 1959). However, such small moduli yield
216 very low seismic velocities, which violate the assumption of Eq. (1). Using the general equation by
217 Ben-Menahem and Singh (1981), the P-wave velocity in this case is estimated to be about 629 m/s or
218 666 m/s, as described in Appendix A. The values are consistent with the estimated near-surface P-wave
219 velocity of the area, ~ 500 m/s, which is close to the sound velocity (Kumagai and Takahashi 1985).
220 Then, the velocities of the S-wave and the surface waves can be smaller than the sound velocity. A generic
221 velocity structure model for volcanic areas (Lesage et al. 2018) also supports the existence of quasi-sonic
222 or subsonic low-velocity layers within tens of meters below the surface. Besides, the incident angle of
223 the airplane noise is not horizontal. Lin and Langston (2009a,b) analyzed seismic and infrasonic data
224 of thunder-induced signals and showed that the ground motion is controlled by the average thickness
225 and velocities of the near-surface layers including the topmost soft and thin layer. We avoid further
226 interpretation of the $(w/p)_{obs}$ for infrasound because of many unknown factors. Nevertheless, it is certain
227 that $(w/p)_{obs}$ for atmosphere-to-ground waves is much smaller than that for ground-to-atmosphere waves.

228 The proposed method has an advantage that it does not use the absolute values of the record.

229 Instruments at permanent monitoring stations are not necessarily well calibrated. The field calibration
230 of an infrasonic station is an issue. Yukutake et al. (2018) made an on-site calibration for the single
231 microphone that recorded the 2015 Hakone eruption. They conducted the calibration after the volcanic
232 activity declined, and found a significant deviation of the microphone response from its specification.
233 On-site calibrations would be more difficult at isolated islands. The seismic stations can be tested using
234 distant earthquakes recorded simultaneously by multiple stations. The same technique is not useful
235 for infrasound, even if there is a good source and enough stations. The spatial amplitude distribution
236 depends significantly on the atmospheric structure (Lacanna et al. 2014), which is also difficult to monitor
237 especially at isolated islands.

238 **Volcanic activity associated with TR1 and TR2**

239 We found that TR1 accompanied infrasound. The infrasound might have coincided with the vent
240 opening or the ejection of large ballistic rocks that were observed from the ground and the sky (Japan
241 Meteorological Agency 2013). The seismic-infrasonic cross-correlation (Fig. 4c) shows a subtle pattern
242 change for a few minutes with TR1. In the power-spectral analysis, we selected the time windows in which
243 the signal might dominate wind noise (step ②). According to the span of the selected time windows, we
244 infer that the explosive activity of the 2013 eruption lasted at least 60 s from 16:01 on April 11.

245 TR2 did not accompany apparent infrasound signals. Matsumoto et al. (2019) reported that remote
246 hydrophones detected no relevant signal on September 12, either, even though small splashes were
247 observed in shallow water near the Okinahama coast. Explosions under shallow water and violent water
248 jets into the air generate detectable infrasound signals (Ichihara et al. 2009; Lyons et al. 2019, 2020), but
249 those were not detected in this case. If an explosion occurs in deep enough water, it may not generate
250 infrasound (Lyons et al. 2019). However, the depth of the splashing zone near the Okinahama coast is less
251 than 10 m. On the other hand, gas emission into the atmosphere by a buoyant plume does not efficiently
252 emanate infrasound (Ichihara et al. 2009). Therefore, we conclude that the unconfirmed 2018 event that
253 generated TR2 was not an explosive eruption either on the ground or undersea.

254 **Conclusions**

255 We have analyzed two volcanic tremor events of Ioto Island, which were TR1 with the 2013 eruption and
256 TR2 with the unconfirmed 2018 activity. The aim was to determine whether the events accompanied
257 infrasound indicating the volcano's surface activity, by a single microphone recorded the events with a co-

258 located seismometer. With a pair of microphone and seismometer, we can sometimes detect infrasound
259 by the seismic-infrasonic cross-correlation method. However, the method was not applicable in the
260 studied case of Ioto Island because seismic activity was intense. Even in such a case, comparing the
261 spectral amplitude ratios $(w/p)_{obs}$ of the events with those of known seismic- and infrasonic- signals gave
262 information.

263 We concluded that TR1 included infrasound, while TR2 did not. The infrasound in the part of TR1
264 might have been excited by the vent opening or the ejection of ballistic rocks. TR2 was not an explosive
265 eruption either on the ground or in the shallow water. If there was any gas (and ash) emission, it might
266 have occurred gently undersea.

267 Infrasonic observation is useful for the detection of eruptions. However, available infrasonic stations
268 are limited at volcanoes on isolated volcanic islands or with less frequent eruption. Using $(w/p)_{obs}$ with a
269 pair of seismic and infrasonic sensors would provide a possibility of extracting infrasound signals covered
270 by seismic signals and wind noise. Because the method refers to $(w/p)_{obs}$ of known signals, it is available
271 without perfect calibrations for the instruments. Concerning to the infrasonic reference signals, we could
272 use various artificial and natural sources like airplane noise, bolide shockwaves, and thunder (Langston
273 2004; Lin and Langston 2007, 2009a).

274 **List of abbreviations**

275 TR1: Tremor associated with an eruption in April 11, 2013 at Ioto Island, TR2: Tremor associated
276 with an unconfirmed activity in September 12, 2018 at Ioto Island, PN: Referenced plane sound, EQ:
277 Referenced tectonic earthquake, CC: Cross-correlation coefficient, $(w/p)_{obs}$: Spectral amplitude ratio
278 between seismic record and infrasonic record, PSD: Power spectral density.

279 **Availability of data and materials**

280 The data set analyzed in this study is not officially available at the request of JMA and JSDF.

281 **Competing interests**

282 The authors declare that they have no competing interest.

283 **Funding**

284 A.K. was financially supported by the Japan Society for the Promotion of Science KAKENHI Grant
285 Number JP 17K14383.

286 **Authors' contributions**

287 AK performed the analysis and drafted the manuscript. MI offered technical support for the present
288 study, and helped with discussion and revision of the manuscript. All authors read and approved the
289 final manuscript.

290 **Acknowledgments**

291 The authors are grateful to the JMA, JSDF, and JVDN for providing data. We also thank Y. Masuda
292 and Y. Kanno who supplied information on the observation condition at Ioto Island.

293 **Appendix A. General solution of pressure-induced surface waves**

294 This appendix mainly refers to Ben-Menahem and Singh (1981) for derivation of equations. Here, we
295 assume that the ground surface is horizontal and take the z -axis vertical upward with $z = 0$ on the
296 surface. The sound speed in the atmosphere is α , and P and SV wave velocities of the ground are α'
297 and β' , respectively. A plane sound wave strikes the ground at an angle e with the z -axis. The angles of
298 transmission for P and SV waves in the ground are e' and f' , respectively. Namely,

$$\hat{c} = \frac{\alpha}{\sin e} = \frac{\alpha'}{\sin e'} = \frac{\beta'}{\sin f'}, \quad (\text{A.1})$$

299 where we define \hat{c} as the apparent wave velocity along the surface.

300 Ben-Menahem and Singh (1981) represented the pressure and vertical velocity at the interface, p^0
301 and w^0 , by the following equations:

$$p^0 = p_{in} \exp \left[i\omega \left(t - \frac{x}{\hat{c}} \right) \right], \quad (\text{A.2})$$

$$w^0 = -p_{in} \frac{m_2}{\rho\alpha} \frac{\cos e}{m_1} \exp \left[i\omega \left(t - \frac{x}{\hat{c}} \right) \right], \quad (\text{A.3})$$

$$m_1 = \cos e \left[\left(\frac{\beta'}{\alpha'} \right)^2 \sin 2e' \sin 2f' + \cos^2 2f' \right], \quad m_2 = \frac{\rho\alpha}{\rho'\alpha'} \cos e',$$

302 where x is the distance along the horizontal component of the wave-incident direction, t is time, ω is the
303 angular frequency, p_{in} is the amplitude of the pressure wave measured on the surface, and ρ and ρ' are
304 the densities of the air and the solid, respectively.

305 On the assumption that the two Lamé's constants (λ, μ) are equal,

$$\frac{\beta'}{\alpha'} = \frac{1}{\sqrt{3}}. \quad (\text{A.4})$$

306 We define a dimensionless parameter:

$$R_p = \frac{\alpha'}{\alpha} \sin e. \quad (\text{A.5})$$

307 Combining Eqs. (A.1)-(A.5), we obtain the dimensionless amplitude ratio,

$$C = \rho' \alpha \frac{w^0}{p^0} = -\sin e \frac{\sqrt{1-R_p^2}}{R_p} \left[\frac{4}{3\sqrt{3}} R_p^2 \sqrt{1-R_p^2} \sqrt{1-\frac{R_p^2}{3}} + \left(1-\frac{2}{3}R_p^2\right)^2 \right]^{-1}. \quad (\text{A.6})$$

308 For most of the case, the seismic velocities of P and SV waves, α' and β' , respectively, are much
309 larger than the sound speed in the air, α . An approximate expression of Eq. (A.6) for $R_p \gg 1$ is given as

$$C \sim -\frac{9}{4R_p^2} \sin e. \quad (\text{A.7})$$

310 For $\sin e = 1$, Eq. (A.7) gives

$$w^0 = \frac{3\alpha}{4\mu} e^{-\frac{i\pi}{2}} p_{in} \exp \left[i\omega \left(t - \frac{x}{\alpha} \right) \right], \quad (\text{A.8})$$

311 which is equivalent with Eq. (1) of the main text for $\lambda = \mu$.

312 As the shallow ground at volcanic areas generally has very low seismic velocities (Lesage et al.
313 2018), the above approximation is not always valid. We calculate Eq. (A.6) to obtain the efficiency of
314 the ground motion induced by a pressure wave, $|C|$, as a function of R_p for $\sin e = 1$. The result is
315 shown in Fig. 7. In our case, pressure-induced surface waves, which are TR1 and PN, have $(w/p)_{obs} \sim$
316 $10 \mu\text{m} \cdot \text{s}^{-1}/\text{Pa}$ as shown in Fig. 6. Therefore, $|C|$ is approximately 4.42 by normalized with $\rho' = 1.16$
317 kg/m^3 and $\alpha = 340 \text{ m}/\text{s}$. This value is obtained with $R_p \sim 0.23, 1.85$ and 1.96 from Fig. 7, if we
318 assume $\sin e = 1$. Then, P-wave velocity becomes $78.2 \text{ m}/\text{s}, 629 \text{ m}/\text{s}$ and $666 \text{ m}/\text{s}$, respectively. The
319 latter two values seem reasonable for the shallow P-wave velocity at a volcanic area (Lesage et al. 2018).

320 Appendix B. General solution of ground-to-air wave

321 Here we consider an incident seismic wave. We do not specify the type of the seismic wave, whether it is
322 a P-wave, a S-wave, or a surface wave. The apparent propagation speed along the surface, \hat{c} , is larger
323 than the actual seismic speed of the ground material unless the wave is propagating horizontally. In the
324 same coordinate system as Appendix A, the vertical velocity of the ground surface at $z = 0$ is assumed
325 as

$$w_0 = w_{in} \exp \left[i\omega \left(t - \frac{x}{\hat{c}} \right) \right]. \quad (\text{B.1})$$

326 We assume that the ground-to-air impedance contrast is infinitely large regardless of the seismic wave
 327 speed due to the density difference. Therefore, Eq. (B.1) is regarded as the boundary condition to the
 328 atmosphere instead of dealing with the acoustic coupling.

329 The wave equation in the air is obtained from the linearized basic equations

$$\frac{\partial \rho}{\partial t} + \rho \nabla \cdot \mathbf{v} = 0, \quad (\text{B.2})$$

330

$$\rho \frac{\partial \mathbf{v}}{\partial t} + \nabla p = 0, \quad (\text{B.3})$$

331

$$\frac{\Delta \rho}{\rho} = \frac{p}{K}, \quad (\text{B.4})$$

332 where \mathbf{v} is the velocity, p is the acoustic pressure, $K \equiv \rho \alpha^2$ is the bulk modulus of the air, and $\Delta \rho$ is
 333 the density change corresponding to the acoustic pressure. By defining the scalar potential ϕ , as
 334 $\mathbf{v} \equiv \nabla \phi$, Eqs. (B.2)-(B.4) are reduced to

$$\frac{\partial^2 \phi}{\partial t^2} - \alpha^2 \nabla^2 \phi = 0. \quad (\text{B.5})$$

335 We assume a solution of Eq. (B.5) in the form of

$$\phi = \Phi \exp(i\omega t - ik_x x - ik_z z), \quad v_z = -ik_z \Phi \exp(i\omega t - ik_x x - ik_z z), \quad (\text{B.6})$$

336 where k_x and k_z are the x - and z - components of the wave number vector in the air, respectively. Using
 337 the boundary condition at $z = 0$ as $v_z = w^0$, which is given in Eq. (B.1),

$$k_x = \frac{\omega}{\hat{c}}, \quad k_z = \sqrt{\frac{\omega^2}{\alpha^2} - k_x^2} = \frac{\omega}{\alpha} \sqrt{1 - \frac{\alpha^2}{\hat{c}^2}}, \quad (\text{B.7})$$

$$\Phi = \frac{w_{in}}{-ik_z}. \quad (\text{B.8})$$

338 Substituting Eqs. (B.6) and (B.8) into Eq. (B.3),

$$p = -\rho \frac{\partial \phi}{\partial t} = p_w \exp(i\omega t - ik_x x - ik_z z), \quad (\text{B.9})$$

339 where the amplitude of the pressure wave, p_w , is specified as

$$p_w = \rho w_{in} \frac{\omega}{k_z} = \frac{\rho \alpha}{\sqrt{1 - \alpha^2/\hat{c}^2}} w_{in}. \quad (\text{B.10})$$

340 When $\alpha/\hat{c} \ll 1$, Eq. (B.10) becomes $p_w = \rho \alpha w_{in}$, which is shown in Eq. (2) of the main text. Seismic
 341 speed of the ground at a shallow depth can be similar or even smaller than α in the case of this study as
 342 explained in Appendix A. However, the very low seismic velocity is expected in the depths smaller than
 343 tens of meters (Lesage et al. 2018). When the seismic velocity propagates from deeper layers, \hat{c} should

344 be larger regardless of the shallow low-velocity layer, considering the velocity continuity. Therefore, the
345 assumption of $\alpha/\hat{c} \ll 1$ is valid. Only when the seismic wave is generated in the shallow low-velocity
346 layer, we may have $\alpha/\hat{c} \geq 1$. Such a shallow seismic source could involve the volcano's surface activity
347 and could generate infrasound waves directly.

348 **References**

- 349 Ben-Menahem A, Singh SJ (1981) Seismic Waves and Sources. 2nd edn, Dover Earth Science Series
- 350 Cannata A, Montalto P, Patane D (2013) Joint analysis of infrasound and seismic signals by cross
351 wavelet transform: detection of Mt. Etna explosive activity. *Natural Hazards and Earth System*
352 *Sciences* 13:1669-677. doi:10.5194/nhess-13-1669-2013
- 353 Cook RK (1971) Infrasound radiated during the Montana earthquake of 1959 August 18. *Geophysical*
354 *Journal International* 26(1-4):191-198. doi:10.1111/j.1365-246X.1971.tb03393.x
- 355 Corwin G, Foster HL (1959) The 1957 explosive eruption on Iwo jima, Volcano Islands. *American*
356 *Journal of Science* 257:161-171
- 357 Dempsey DE, Cronin SJ, Mei S, Kempa-Liehr AW (2020) Automatic precursor recognition and
358 real-time forecasting of sudden explosive volcanic eruptions at Whakaari, New Zealand. *Nature*
359 *Communications* 11:3562. doi.org/10.1038/s41467-020-17375-2
- 360 Donn WL, Posmentier ES (1964) Ground-coupled air waves from the great Alaskan earthquake. *Journal*
361 *of Geophysical Research* 69(24):5357-5361. doi:10.1029/JZ069i024p05357
- 362 Fee D, Garces M (2007) Infrasonic tremor in the diffraction zone. *Geophysical Research Letters*
363 34(16):L16826. doi:10.1029/2007GL030616
- 364 Ichihara M, Ripepe M, Goto A, Oshima H, Aoyama H, Iguchi M, Tanaka K, Taniguchi H (2009)
365 Airwaves generated by an underwater explosion: Implications for volcanic infrasound. *Journal of*
366 *Geophysical Research* 114(B3):B03210. doi:10.1029/2008JB005792
- 367 Ichihara M, Takeo M, Yokoo A, Oikawa J, Ohminato T (2012) Monitoring volcanic activity using
368 correlation patterns between infrasound and ground motion. *Geophysical Research Letters*
369 39(4):L04304. doi:10.1029/2011GL050542
- 370 Ichihara M (2016) Seismic and infrasonic eruption tremors and their relation to magma discharge rate:
371 A case study for sub-Plinian events in the 2011 eruption of Shinmoe-dake, Japan. *Journal of*
372 *Geophysical Research: Solid Earth* 121(10):7101-7118. doi:10.1002/2016JB013246

373 Japan Meteorological Agency (2013) Monthly Volcanic Activity Report (April 2013) (in Japanese)

374 Japan Meteorological Agency (2018) Monthly Volcanic Activity Report (April 2018) (in Japanese)

375 Kaizuka S, Kato S, Nagaoka S, Miyauchi T (1985) Geomorphology of Iwo-jima and surrounding sea
376 floor. *Journal of Geography (Chigaku Zasshi)* 94(6):424-436. doi:10.5026/jgeography.94.424 (in
377 Japanese with English abstract)

378 Kaneko T, Maeno F, Yasuda A, Takeo M, Takasaki K (2019) The 2017 Nishinoshima eruption:
379 combined analysis using Himawari-8 and multiple high-resolution satellite images. *Earth, Planets and
380 Space* 71:140. doi:10.1186/s40623-019-1121-8

381 Kim TS, Hayward C, Stump B (2004) Local infrasound signals from the Tokachi-Oki earthquake.
382 *Geophysical Research Letters* 31:L20605. doi:10.1029/2004GL021178

383 Kumagai T, Takahashi H (1985) Seismic wave velocity structure beneath the Iwo-jima volcanoes.
384 *Journal of Geography (Chigaku Zasshi)* 94(6):545-550. doi:10.5026/jgeography.94.545 (in Japanese
385 with English abstract)

386 Lacanna G, Ichihara M, Iwakuni M, Takeo M, Iguchi M, Ripepe M (2014) Influence of atmospheric
387 structure and topography on infrasonic wave propagation. *Journal of Geophysical Research: Solid
388 Earth* 119:2988-3005. doi:10.1002/2013JB010827

389 Langston CA (2004) Seismic ground motions from a bolide shock wave. *Journal of Geophysical
390 Research* 109: B12309. doi:10.1029/2004JB003167

391 Lesage P, Heap MJ, Kushnir A (2018) A generic model for the shallow velocity structure of volcanoes.
392 *Journal of Volcanology and Geothermal Research* 356:114-126. doi:10.1016/j.jvolgeores.2018.03.003

393 Lin T-L, Langston CA (2007) Infrasound from thunder: A natural seismic source. *Geophysical Research
394 Letters* 34:L14304. doi:10.1029/2007GL030404

395 Lin T-L, Langston CA (2009a) Thunder-induced ground motions: 1. Observations. *Journal of
396 Geophysical Research* 114:B04303. doi:10.1029/2008JB005769

397 Lin T-L, Langston CA (2009b) Thunder-induced ground motions: 2. Site characterization. *Journal of
398 Geophysical Research* 114:B04304. doi:10.1029/2008JB005770

399 Lo Presti DCF, Jamiolkowski M, Pallara O, Cavallaro A, Pedroni S (1997) Shear modulus and damping
400 of soils. *Geotechnique* 47(3):603-617. doi:10.1680/geot.1997.47.3.603

401 Lyons JJ, Haney MM, Fee D, Wech AG, Waythomas C (2019) Infrasound from giant bubbles during
402 explosive submarine eruptions. *Nature Geoscience* 12:952-958. doi:10.1038/s41561-019-0461-0

403 Lyons JJ, Lezzi AM, Fee D, Schwaiger HF, Wech AG, Haney MM (2020) Infrasound generated by the
404 2016-2017 shallow submarine eruption of Bogoslof volcano, Alaska. *Bulletin of Volcanology* 82:19.
405 doi:10.1007/s00445-019-1355-0

406 Maeno F, Nakada S, Kaneko T (2016) Morphological evolution of a new volcanic islet sustained by
407 compound lava flows. *Geology* 44(4):259-262. doi:10.1130/G37461.1

408 Mastin LG, Witter JB (2000) The hazards of eruptions through lakes and seawater. *Journal of*
409 *Volcanology and Geothermal Research* 97:195-214. doi:10.1016/S0377-0273(99)00174-2

410 Matoza RS, Fee D (2014) Infrasonic component of volcano-seismic eruption tremor. *Geophysical*
411 *Research Letters* 41:1964-1970. doi:10.1002/2014GL059301

412 Matsumoto H, Zampolli M, Haralabus G, Stanley J, Mattila J, Özel, NM (2019) Interpretation of
413 detections of volcanic activity at Ioto Island obtained from in situ seismometers and remote
414 hydrophones of the International Monitoring System. *Scientific Reports* 9:19519.
415 doi:10.1038/s41598-019-55918-w

416 McKee K, Fee D, Haney M, Matoza RS, and Lyons J (2018) Infrasound signal detection and back
417 azimuth estimation using ground - coupled airwaves on a seismo - acoustic sensor pair. *Journal of*
418 *Geophysical Research: Solid Earth* 123:6826-6844. doi:10.1029/2017JB015132

419 Nishida K, Ichihara M (2015) Real-time infrasonic monitoring of the eruption at a remote island
420 volcano using seismoacoustic cross correlation. *Geophysical Journal International* 204:748-752.
421 doi:10.1093/gji/ggv478

422 Notsu K, Sugiyama K, Hosoe M, Uemura A, Shimoike Y, Tsunomori F, Sumino H, Yamamoto J, Mori
423 T, Hernandez PA (2005) Diffuse CO₂ efflux from Iwojima volcano, Izu-Ogasawara arc, Japan.
424 *Journal of Volcanology and Geothermal Research* 139:147-161. doi:10.1016/j.jvolgeores.2004.08.003

425 Perttu A, Caudron C, Assink JD, Metz D, Tailpied D, Perttu B, Hibert C, Nurfiani D, Pilger C, Muzli
426 M, Fee D, Andersen OL, Taisne B (2020) Reconstruction of the 2018 tsunamigenic flank collapse and
427 eruptive activity at Anak Krakatau based on eyewitness reports, seismo-acoustic and satellite
428 observations. *Earth and Planetary Science Letters* 541:116268. doi:10.1016/j.epsl.2020.116268

429 Ripepe M, Marchetti E, Delle Donne D, Genco R, Innocenti L, Lacanna G, and Valade S (2018)
430 Infrasonic early warning system for explosive eruptions. *Journal of Geophysical Research* 123
431 (11):9570-9585. doi:10.1029/2018JB015561

432 Shields FD (2005) Low-frequency wind noise correlation in microphone arrays. *The Journal of the*

433 Acoustical Society of America 117:3489, doi:10.1121/1.1879252
434 Stix J, Moor JM (2018) Understanding and forecasting phreatic eruptions driven by magmatic
435 degassing. *Earth, Planets and Space* 70:83, doi:10.1186/s40623-018-0855-z
436 Ueda H, Nagai M, Tanada T (2018) Phreatic eruptions and deformation of Ioto Island (Iwo-jima),
437 Japan, triggered by deep magma injection. *Earth, Planets and Space* 70:38.
438 doi:10.1186/s40623-018-0811-y
439 Watada S, Kunugi T, Hirata K, Sugioka H, Nishida K, Sekiguchi S, Oikawa J, Tsuji Y, Kanamori H
440 (2006) Atmospheric pressure change associated with the 2003 Tokachi-Oki earthquake. *Geophysical*
441 *Research Letters* 33:L24306. doi:10.1029/2006GL027967
442 Williams R, Rowley P, Garthwaite MC (2019) Reconstructing the Anak Krakatau flank collapse that
443 caused the December 2018 Indonesian tsunami. *Geology* 47:973-976. doi:10.1130/G46517.1
444 Yukutake Y, Ichihara M, Honda R (2018) Infrasonic wave accompanying a crack opening during the
445 2015 Hakone eruption. *Earth, Planets and Space* 70:53. doi:10.1186/s40623-018-0820-x

446 **Preparing illustrations and figures**

Figure 1. Map of Ioto Island with the station locations shown by open circles. The triangle in the inset marks the location of Ioto Island in Japan. IOCD has a seismometer and a microphone, of which data are mainly used in this study. IJSV and IJTV are seismic stations. The 2013 eruption and water spouts accompanied by the 2018 activity occurred at Million dollar hole and in shallow water near Okinahama coast marked with crosses, respectively (Japan Meteorological Agency 2013, 2018).

Figure 2. Vertical ground velocity of TR1 on April 11, 2013, and TR2 on September 12, 2018. (a, b) The raw records at IOCD (black), IJSV (yellow), and IJTV (blue). (c, d) The spectrograms for the data at IOCD. The color bars indicate the power in $\text{dB} = 10 \log_{10}(\text{PSD}/\text{PSD}_{\text{ref}})$ with $\text{PSD}_{\text{ref}} = 1 \text{ (m}\cdot\text{s}^{-1})^2/\text{Hz}$.

Figure 3. Power spectral features of tremors (magenta) and background noise (black). The symbols show the values of the meaningful frequency bands selected by step ⑤ of the text. (a, b) The upper magenta line with the upward triangles is P_W , and the associated black line is P_W^b , on the left axis. The lower magenta line with inverted triangles is P_P , and the associated black line is P_P^b , on the right axis. (c, d) The spectral amplitude ratio between seismic record and infrasonic record, $(w/p)_{obs}$, as a function of frequency. The horizontal dashed line indicates the theoretical value for the ground-to-atmosphere wave calculated by Eq. (2) with $\alpha = 340$ m/s and $\rho = 1.16$ kg/m³.

Figure 4. (a, b) TR1 and TR2 waveforms recorded at IOCD. The black shows the vertical component of the seismometer, and the magenta shows the microphone record. The data were filtered within the frequency band of 1-10 Hz. (c, d) The cross-correlation of the seismic and infrasonic data in (a, b) in a 5-s time window sliding every 1 s. The vertical axis, τ , is the time delay of the seismic to infrasonic data.

Figure 5. a, b) PN and EQ waveforms recorded at IOCD on September 12 and 18, 2018, respectively. The black shows the vertical component of the seismometer, and the magenta shows the microphone record. PN and EQ data are filtered within the frequency band of 10-30 Hz and 1-10 Hz, respectively. (c, d) The cross-correlation of the seismic and infrasonic data in (a, b) in a 5-s time window sliding every 1 s. The vertical axis, τ , is the time delay of the seismic to infrasonic data.

Figure 6. The same plots of tremors (magenta) as in Figure 3, compared with the corresponding values of EQ (black) and PN (blue).

Figure 7. The absolute value of C vs. R_p in the case of $\sin e = 1$.

Figures

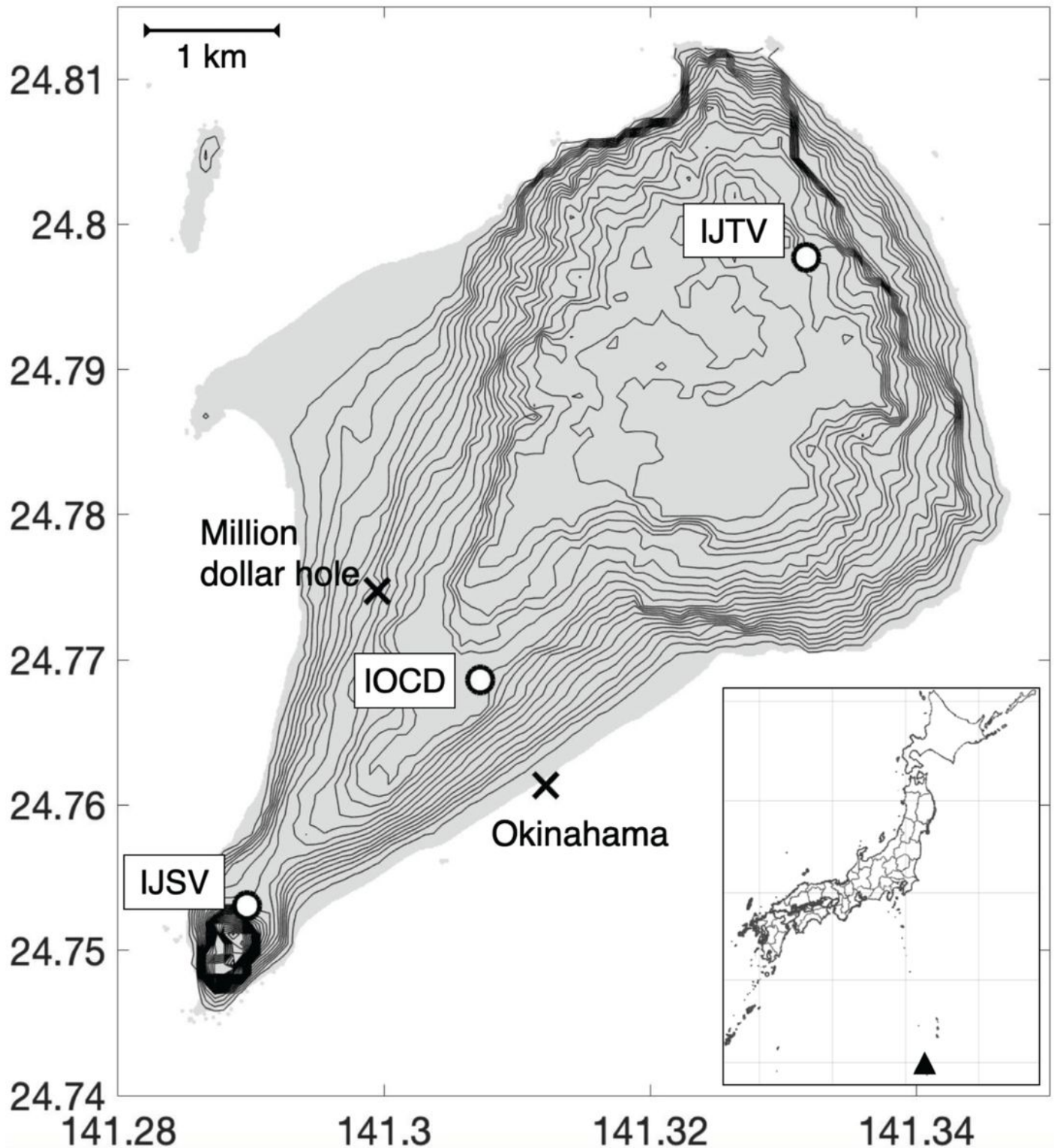


Figure 1

Map of Ioto Island with the station locations shown by open circles. The triangle in the inset marks the location of Ioto Island in Japan. IOCD has a seismometer and a microphone, of which data are mainly used in this study. IJSV and IJTV are seismic stations. The 2013 eruption and water spouts accompanied

by the 2018 activity occurred at Million dollar hole and in shallow water near Okinahama coast marked with crosses, respectively (Japan Meteorological Agency 2013, 2018).

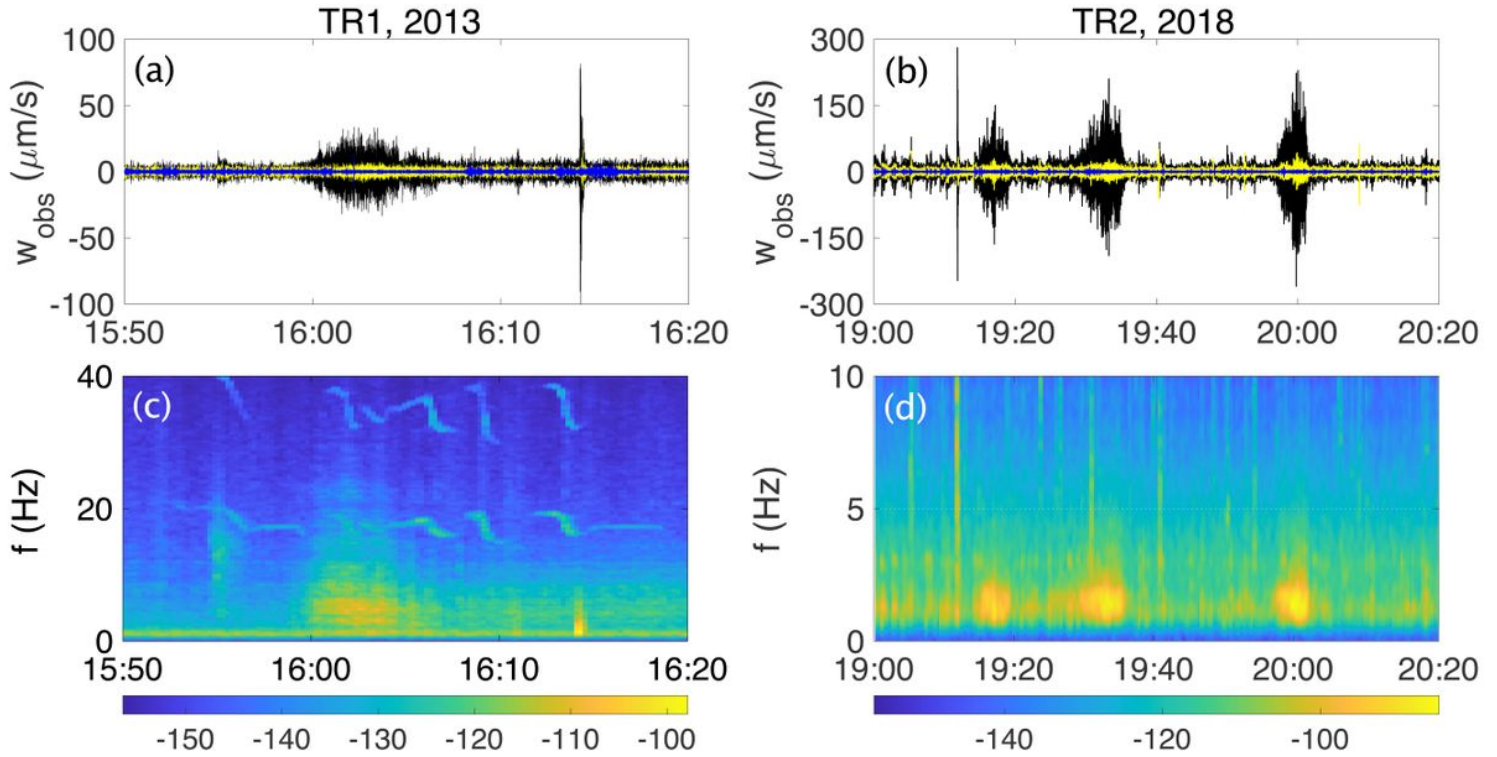


Figure 2

Vertical ground velocity of TR1 on April 11, 2013, and TR2 on September 12, 2018. (a, b) The raw records at IOCD (black), IJSV (yellow), and IJTV (blue). (c, d) The spectrograms for the data at IOCD. The color bars indicate the power in dB = $10 \log_{10}(\text{PSD}/\text{PSD}_{\text{ref}})$ with $\text{PSD}_{\text{ref}} = 1 (\text{m}\cdot\text{s}^{-1})^2/\text{Hz}$.

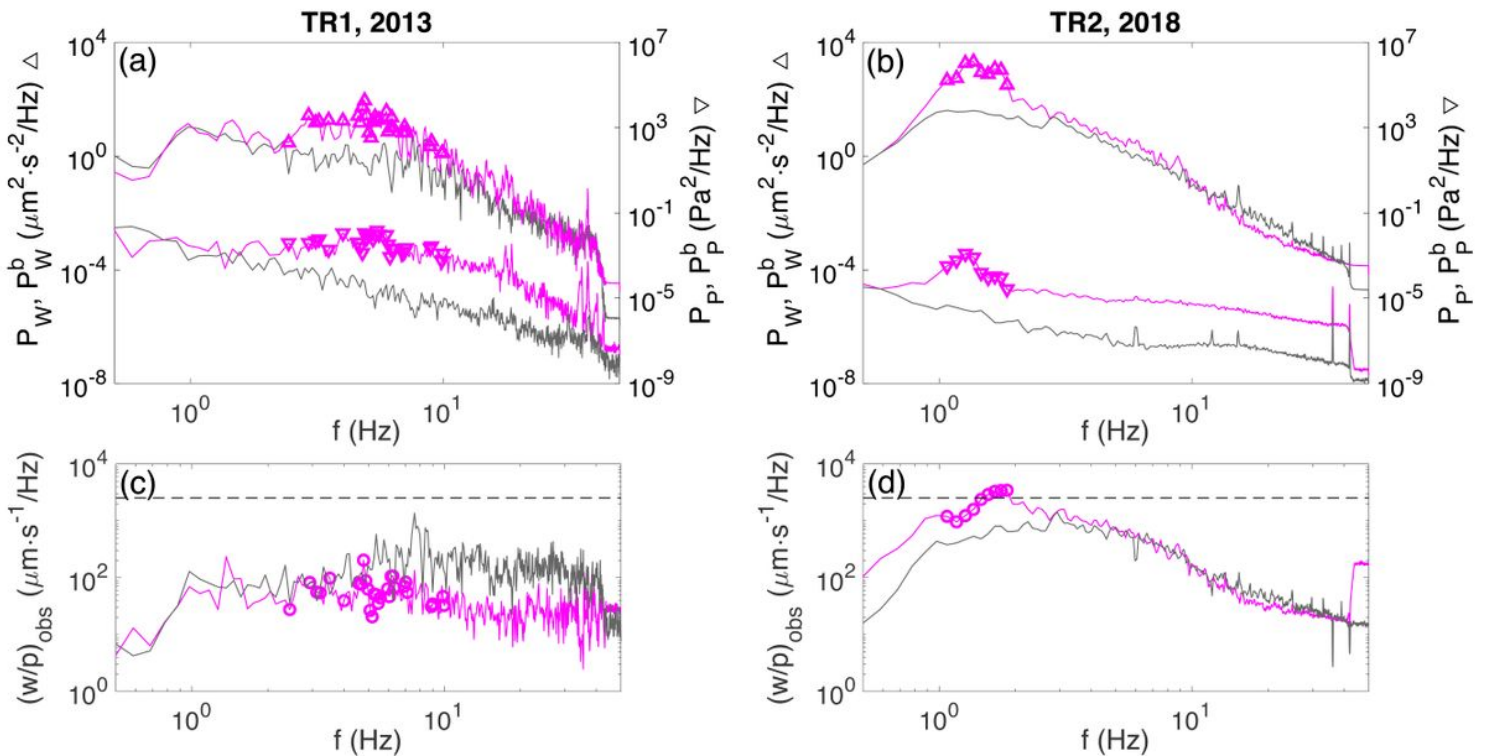


Figure 3

Power spectral features of tremors (magenta) and background noise (gray). The symbols show the values of the meaningful frequency bands selected by step 5 of the text. (a, b) The upper magenta line with the upward triangles is PW, and the associated gray line is PWb, on the left axis. The lower magenta line with inverted triangles is PP, and the associated gray line is PPb, on the right axis. (c, d) The spectral amplitude ratio between seismic record and infrasonic record, $(w/p)_{obs}$, as a function of frequency. The horizontal dashed line indicates the theoretical value for the ground-to-atmosphere wave calculated by equation (2) with $C_a = 340$ m/s and $\rho = 1.16$ kg/m.

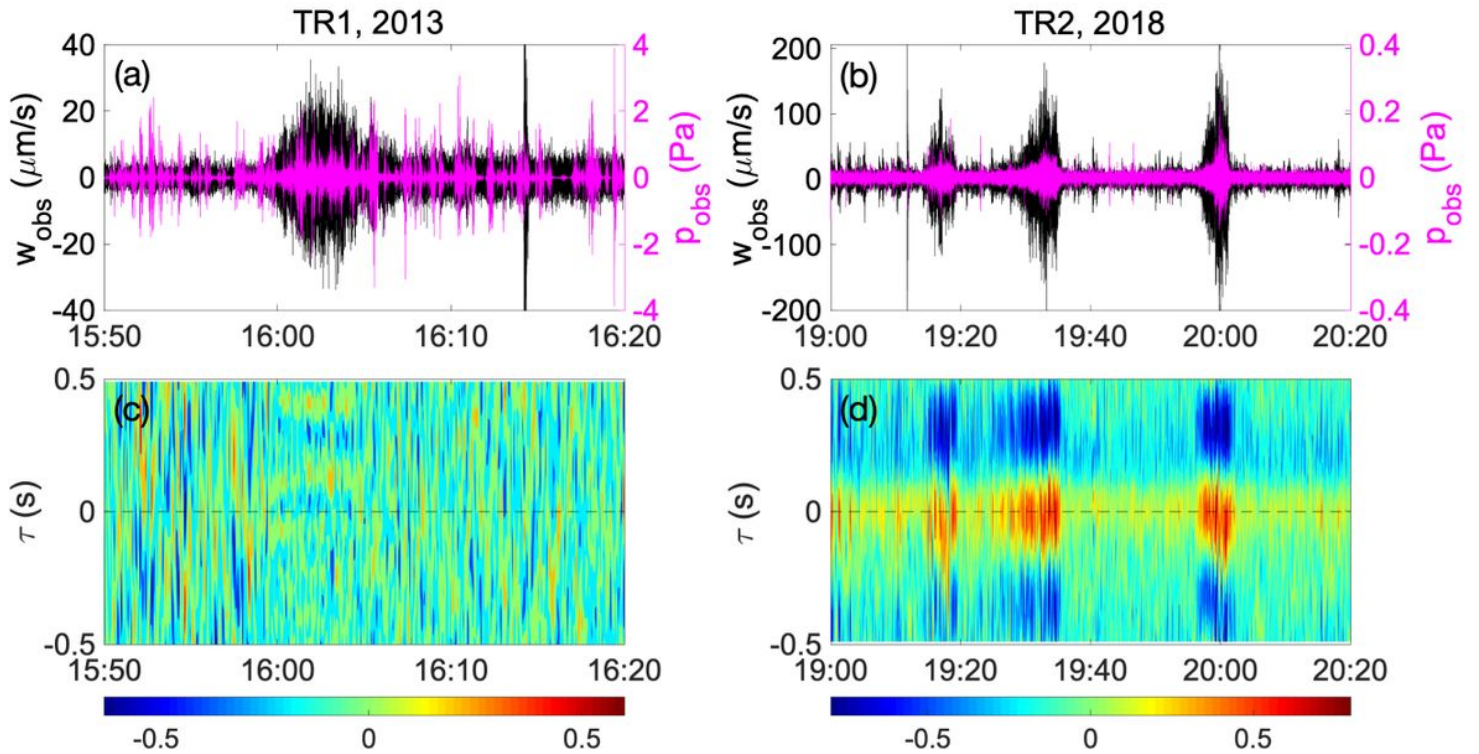


Figure 4

(a, b) TR1 and TR2 waveforms recorded at IOCD. The black shows the vertical component of the seismometer, and the magenta shows the microphone record. The data were filtered within the frequency band of 1-10 Hz. (c, d) The cross-correlation of the seismic and infrasonic data in (a, b) in a 5-s time window sliding every 1 s. The vertical axis, τ , is the time delay of the seismic to infrasonic data.

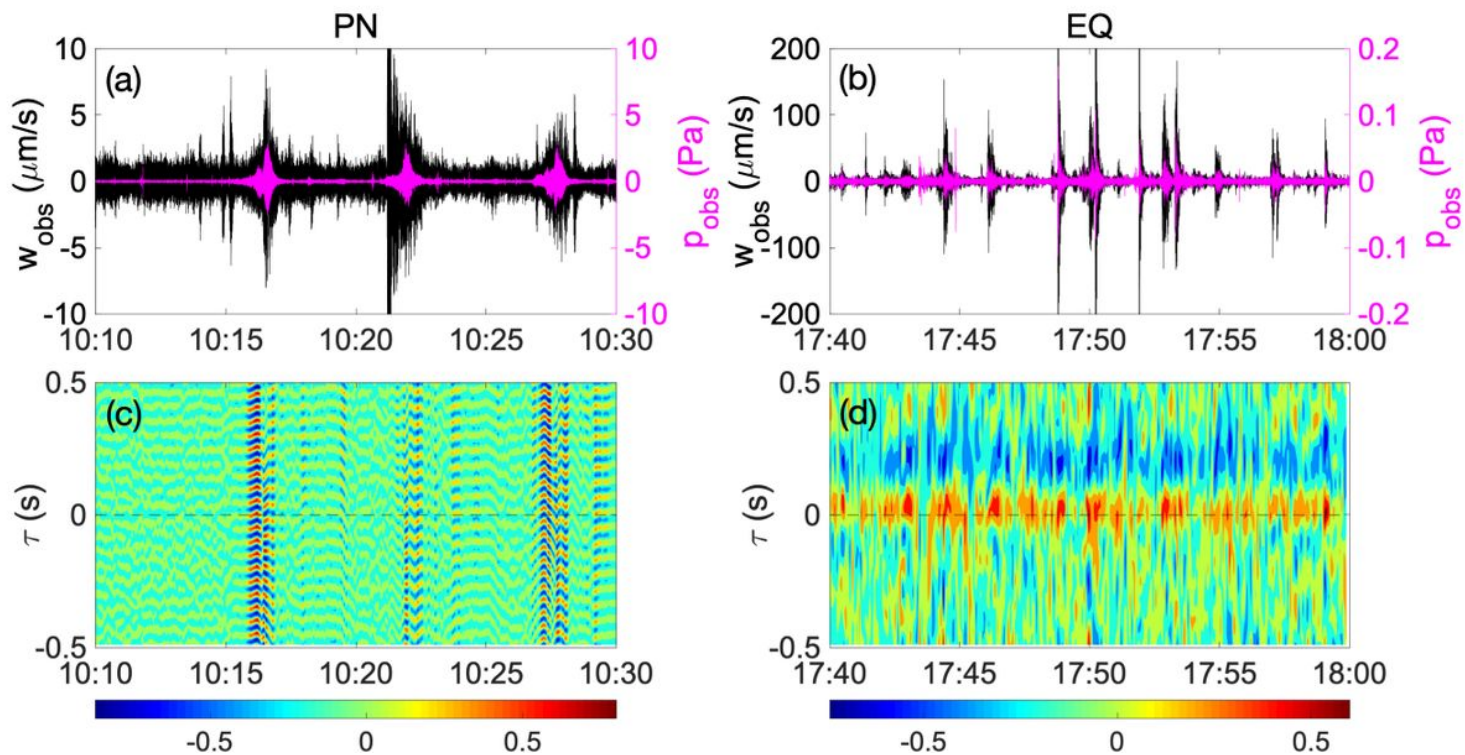


Figure 5

a, b) PN and EQ waveforms recorded at IOCD on September 12 and 18, 2018, respectively. The black shows the vertical component of the seismometer, and the magenta shows the microphone record. PN and EQ data are filtered within the frequency band of 10-30 Hz and 1-10 Hz, respectively. (c, d) The cross-correlation of the seismic and infrasonic data in (a, b) in a 5-s time window sliding every 1 s. The vertical axis, τ , is the time delay of the seismic to infrasonic data.

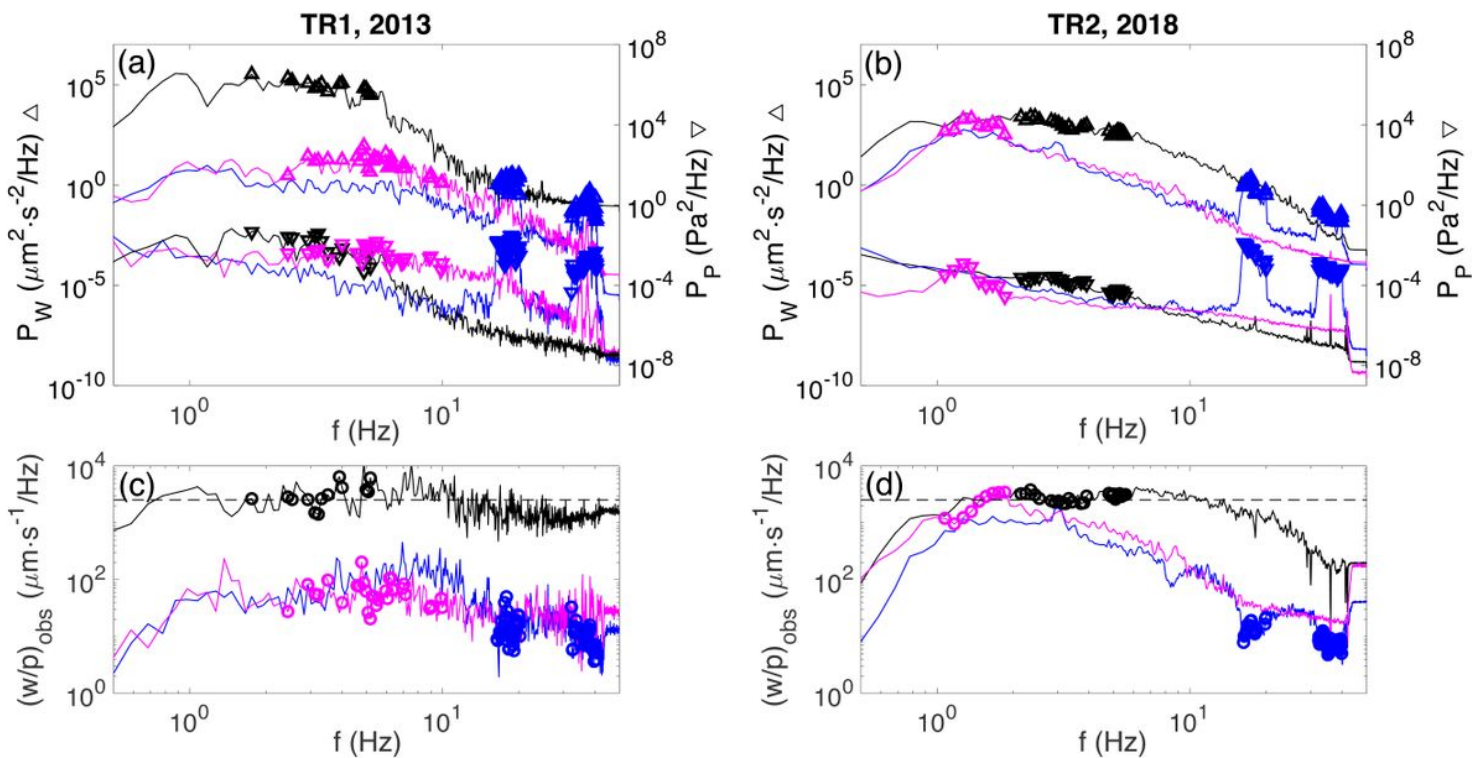


Figure 6

The same plots of tremors (magenta) as in Figure 3, compared with the corresponding values of EQ (black) and PN (blue).

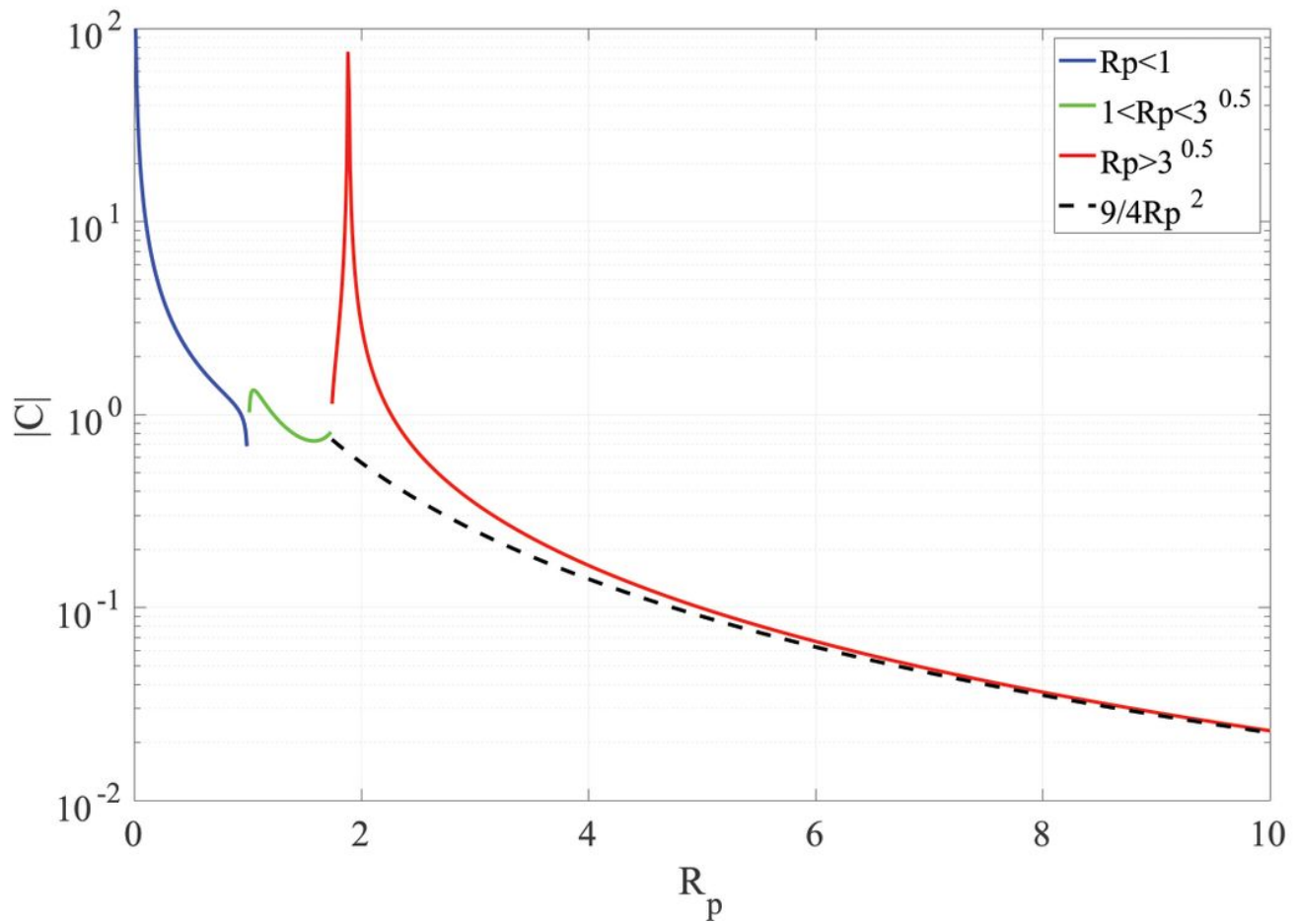


Figure 7

The absolute value of C vs. R_p in the case of $\sin e = 1$.

Supplementary Files

This is a list of supplementary files associated with this preprint. Click to download.

- [SuppEQtimetable.xlsx](#)